

A Zero-Threshold PT-Symmetric Polariton-Raman Laser

Avijit Dhara^{1†}, Pritam Das^{1†}, Devarshi Chakrabarty^{1†}, Kritika Ghosh², Ayan Roy Chaudhuri², Sajal Dhara^{1*}

¹*Department of Physics, IIT Kharagpur, Kharagpur-721302, India*

²*Materials Science Centre, IIT Kharagpur, Kharagpur-721302, India*

[†] *These authors contributed equally*

^{*} *Corresponding author. email: sajaladhara@phy.iitkgp.ac.in*

Abstract: Parity-time (PT) symmetry in a non-Hermitian framework can be harnessed for numerous applications in optics such as laser mode selection, non-reciprocal light propagation, polaritonic optical switches, and enhanced sensing. Here we show a zero-threshold Raman laser can be achieved in an anisotropic optical microcavity in the PT-symmetry broken phase via polarization selective optical pumping. A loss-gain mechanism between two polarized Stokes modes arises naturally via polarization dependent stimulated scattering and anisotropic Raman gain of the active layered material inside the microcavity. A microscopic theory of stimulated Raman process in anisotropic microcavity successfully explains our results at various temperatures and enabled us to predict the parameters of a proposed quantum PT-symmetric Hamiltonian. Our realization of the zero-threshold Raman laser and the proposed theory of stimulated Raman scattering in anisotropic microcavity can lead to future development of novel technologies such as efficient quantum frequency converters for applications in quantum photonics and information.

Ultralow-threshold Raman lasers in semiconductors [1–3] are promising for their potential applications as frequency tunable coherent light sources. A zero-threshold Raman laser which has remained unattained so far could lead to novel technologies for quantum photonics which is beyond any existing finite threshold Raman laser. One such application of zero-threshold Raman laser would be to realize an efficient quantum frequency converter for non-classical light sources including single photons with frequency tunability range not accessible to present technologies [4]. Hence, a zero-threshold Raman laser can be promising for on-chip quantum photonics and quantum communications. Microcavity polariton systems are recently being utilized for engineering non-Hermitian topology of polaritonic bands [5–12]. A class of non-Hermitian systems which remain invariant under parity-time (PT) inversion can possess real eigenvalues, facilitating several useful and non-trivial functionalities like single-mode or chiral lasing and non-reciprocal light propagation [13–21]. In this work we demonstrate a single mode zero-threshold Raman laser in an anisotropic optical microcavity by driving the system into a PT-symmetry broken phase by optical pumping. We utilize the strong Raman emission of layered ReS₂ with intriguing optical anisotropy resulting in polarized Stokes modes that can be tunable in resonance with the exciton-polaritons. The loss and gain mechanism in this non-Hermitian system arises naturally via polarization dependent stimulated Raman process and anisotropic Raman gain of the active layered material inside the microcavity. A microscopic theory of stimulated Raman scattering has been developed which agrees well with our experimental results and identifies the parameters of the phenomenological description of our results with a non-Hermitian Hamiltonian. Therefore, our work carries two significant advances, first, the experimental realization of a zero-threshold Raman laser and second, the development of a theoretical understanding of stimulated Raman scattering in anisotropic microcavity which can be applied to engineer polarization-controlled light-matter interactions for quantum technologies.

Two dimensional semiconductors like Rhenium disulphide (ReS_2) are being recognized as a potential active laser medium and an ideal platform for realising exciton-polaritons [22–26]. ReS_2 is known for its distorted 1T crystal structure hosting strongly polarized excitons [27,28], with tunable light-matter coupling [29]. The ReS_2 -embedded microcavity supports two sets of non-orthogonal exciton-polariton modes with polarization tunable dispersions. Such systems are being understood recently using non-Hermitian descriptions [30–38]. Due to reduced crystal symmetry, ReS_2 has 18 Raman modes in the range of 100 to 450 cm^{-1} [39]. Interestingly we observed the presence of dominant Raman peaks and vanishing photoluminescence at near resonance excitation similar to what has been reported recently in ReS_2 [40], which makes it a unique platform to observe Raman lasing. The ReS_2 -microcavity polaritonic system can thus be pumped to achieve polarization dependent stimulated resonant Raman scattering [41,42].

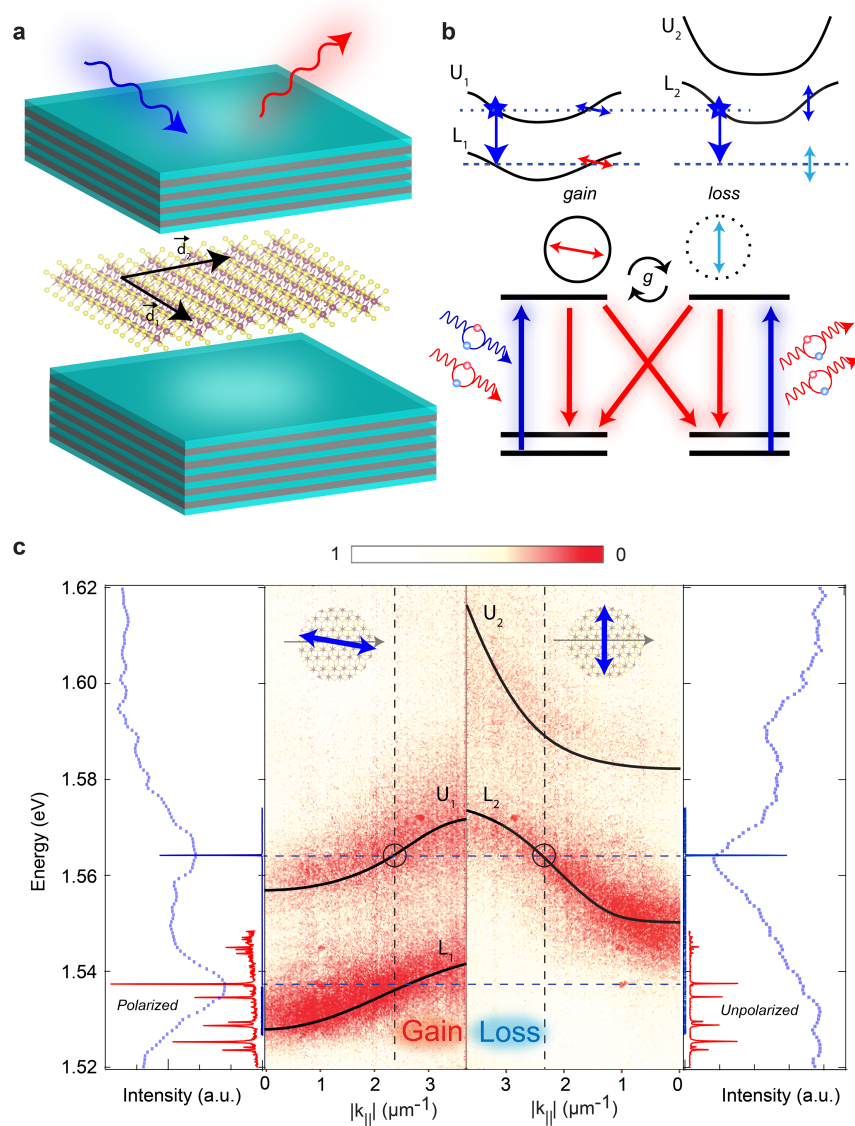


Fig. 1. Schematic and experimental data rendering the mechanism of zero threshold polariton Raman laser and PT-symmetry. **a.** Schematic of ReS_2 embedded in a microcavity showing the two near-orthogonal directions d_1 and d_2 where d_1 is parallel to the b-axis. **b.** Simplified schematic of the stimulated Raman scattering processes involving a pair of polariton dispersions polarized along d_1 and d_2 . The system is pumped at an energy such that

both d_1 and d_2 polarized pump components are resonant with a polariton mode, while the d_1 (d_2) polarized Stokes-shifted Raman emission coincides with a polariton mode (stop band) thus experiencing gain (loss). These non-orthogonal Stokes-shifted states couple with each other, creating a PT-symmetric system. **c.** Left (right) panel shows angle-resolved reflectance revealing polariton dispersions probed by linearly polarized light along d_1 (d_2) indicated by double sided arrow w.r.t. crystal b-axis. EPs in the polariton bands are marked by a black circle. Extreme left (right) panel shows the Raman spectra overlayed with the reflectance cross-section across the EP obtained from the angle resolved data for pump polarization d_1 (d_2). Pump laser spectrum is shown near the EP (in blue, intensity in arbitrary scale).

A 10 nm thick ReS₂ crystal is mechanically exfoliated and placed in an optical microcavity (see Methods for fabrication details), as illustrated in Fig. 1a. The biaxiality of ReS₂ splits the transverse electric (TE) and transverse magnetic (TM) cavity modes, which interact with two nearly orthogonal anisotropic excitons, (X_1 and X_2). This interaction leads to the formation of exciton-polariton pairs, as shown in the schematic in Fig. 1b (see Note S1 in Supplementary Material for details). The four resulting polariton modes are designated as X_1 upper (U_1), X_1 lower (L_1), X_2 upper (U_2), and X_2 lower (L_2) branches [7]. The microscopic mechanisms of stimulated Raman scattering resulting in two

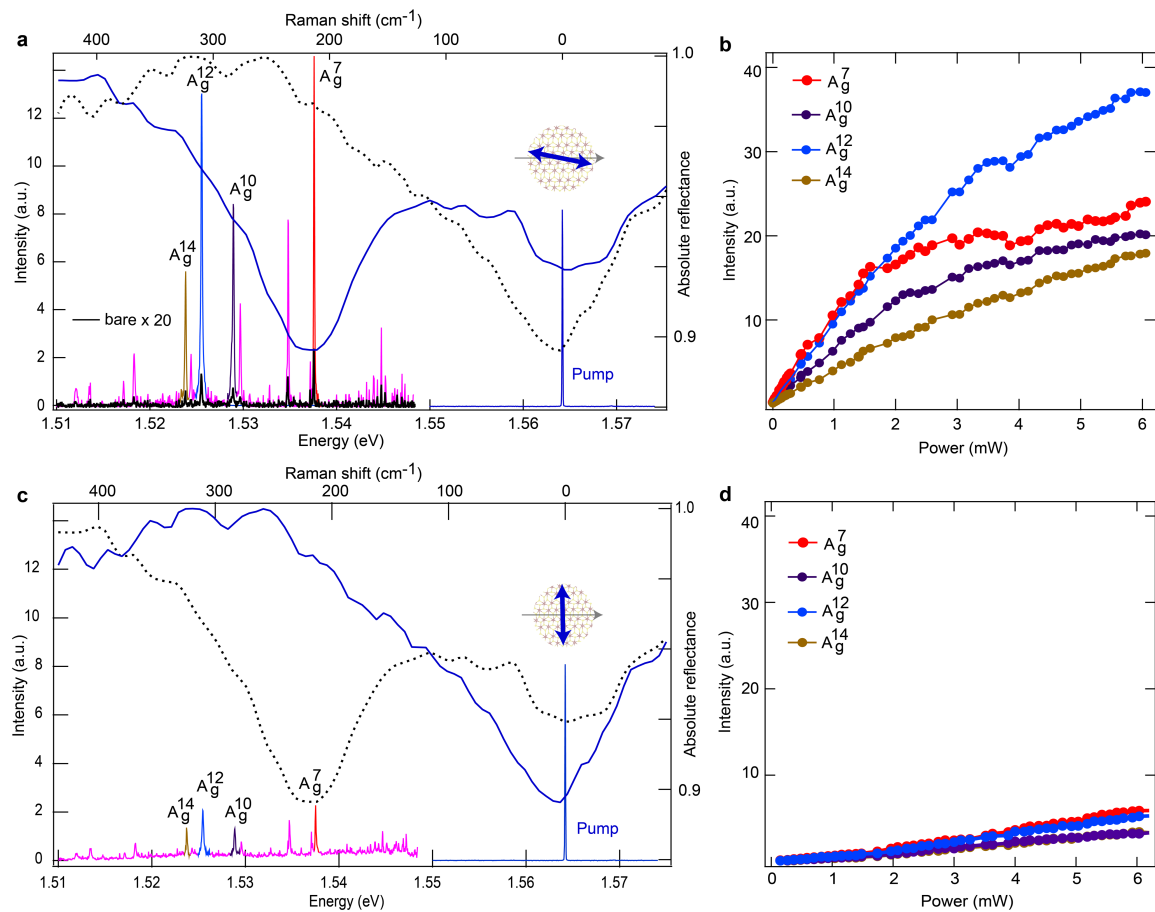


Fig. 2. Polariton Raman laser power dependence at 4 K. **a.** Emission spectrum for d_1 polarized pump with energy 1.564 eV, overlaid with the angle-resolved reflectance (dotted line) for d_1 polarized light across the EP (where it is pumped). Four distinct Raman modes are labelled with different colours. Raman spectra from bare ReS₂/SiO₂ (black, multiplied 20X) is shown for comparison. **b.** Power dependence for d_1 polarized pump with analyzer kept along d_1 showing zero threshold characteristics for all four Raman modes. **c, d.** Same as **a, b** for d_2 polarized pump, with analyzer kept along d_2 . Reflectance line plots are overlayed for both d_1 and d_2 polarized polaritons.

polarized Stokes modes which are coupled due to the off-diagonal Raman gain (g_{12}, g_{21}) are shown schematically in the lower panel in Fig. 1b. We define two non-orthogonal polarization directions with respect to the crystallographic b-axis, 170° (d_1) and 90° (d_2) corresponding to the absorption maxima attributed to X_1 and X_2 polariton branches respectively. Polarization and angle resolved reflectivity measured at 4 K (see Methods in Supplemental Material and reference [43] therein) reveals the pair of polaritons, as shown in Fig. 1c where the crystallographic b-axis is oriented along k_{\parallel} . There exists a point in the polariton dispersion (marked with circles in Fig. 2c) where the U_1 and L_2 branches coalesce which is the Exceptional Point (EP) of the polariton system (see Methods in Supplemental Material). We have chosen the pump beam energy at the EP (at 1.564 eV) to get equal amplifications of the pump beam for both the polarization modes d_1 and d_2 inside microcavity. Plot in the left extreme in Fig. 1c shows strong emission due to Raman lasing when the pump beam is polarized along d_1 , and the Stokes lines lies within the L_1 band of the polaritons. The Raman intensity reduces drastically as shown in the right extreme in Fig. 1c when the pump is polarized along d_2 , and the Stokes lines lies in the stop band of the cavity. To understand the results in more detail the Raman spectrum and power dependence are discussed below.

Several Raman modes are identified from existing literature of bare ReS_2 with AA stacking order (see Note S2 and Fig. S1 in Supplemental Material and reference [44] therein). Out of these Raman peaks we focus on four lines labeled by different colours: A_g^7 (214 cm^{-1}), A_g^{10} (284 cm^{-1}), A_g^{12} (311 cm^{-1}) and A_g^{14} (325 cm^{-1}) as shown in Fig. 2a-2c. We find the Raman emission is amplified by ~ 150 - 300 times compared to bare ReS_2 when the pump is polarized along d_1 (shown in Fig. 2a). The tunability and intensity variation of the Raman lines with pump wavelength is shown in Supplemental Material Fig. S2. The spectral linewidths ($\sim 0.5 \text{ \AA}$) of these Raman peaks are within the spectrometer resolution. The amplified Raman intensity is highly polarized and shows a linear power dependence (down to 180 nW, see Supplemental Material Fig. S3) which gets saturated at higher power, revealing the signature of zero-threshold lasing as shown in Fig 2b. A similar power dependence was reported earlier in trapped single atom laser from microcavity [45]. A zero threshold laser can be characterized by the value of spectral overlap factor β between the Raman gain profile and polariton mode in frequency domain being unity [46–50] (see Note S4 in the Supplemental Material for comparison between conventional and polariton-Raman laser). For d_1 polarized pump, the Stokes modes are resonant with the lower polariton L_1 , thus experiencing amplification due to Purcell enhancement. Conversely, for d_2 polarized pump, the Stokes modes fall within the stop band of the cavity, thus experiencing relative loss resulting in reduced intensity of partially polarized Raman emission as shown in Fig. 2c-d. Here the polarized Stokes modes can be considered as a two state system governed by a non-Hermitian PT-symmetric Hamiltonian which is similar to two spatially separated weakly coupled systems with loss and gain investigated earlier in the literature [12,14,16]. We show that in the PT symmetry broken phase, the system can achieve single-mode selectivity, ensuring $\beta \rightarrow 1$, the condition for zero-threshold laser as discussed below.

The variation of the polarization-resolved intensity and the state of polarization of the Raman emissions sheds light into further understanding of the microscopic mechanisms. In Fig. 3a (at 4 K) and Fig. 3b (at 300 K) we plot the polarized intensity components of the Raman signal measured along the d_1 and d_2 directions by an analyzer while varying the polarization of the pump beam (θ). At $\theta = 0^\circ$ (d_1 pump polarization), the emission intensity is highest for the d_1 Stokes mode exhibiting a strong degree of polarization > 0.95 with major axis aligned along d_1 polarization (see Fig. 3a, top inset). As the pump polarization rotates from d_1 to d_2 ($\theta \sim 90^\circ$), the overall Raman emission intensity of d_1 mode reduces but it remains much higher than the d_2 mode. What is more counterintuitive is that the degree of polarization reduces significantly to < 0.4 at $\theta \sim 90^\circ$ as shown in the right inset in Fig. 3a.

The same θ variation of d_1 and d_2 components of the Stokes mode show very different characteristics at 300 K as shown in Fig. 3b, where the intensities of d_1 and d_2 components cross each other at $\theta \sim 60^\circ$. We show below that such counterintuitive polarization variation of the d_1 and d_2 components and their temperature variation can be understood in the framework of non-Hermitian PT-symmetry. We further demonstrate that a microscopic theory can predict the temperature dependent parameters of our proposed PT-symmetric Hamiltonian as follows.

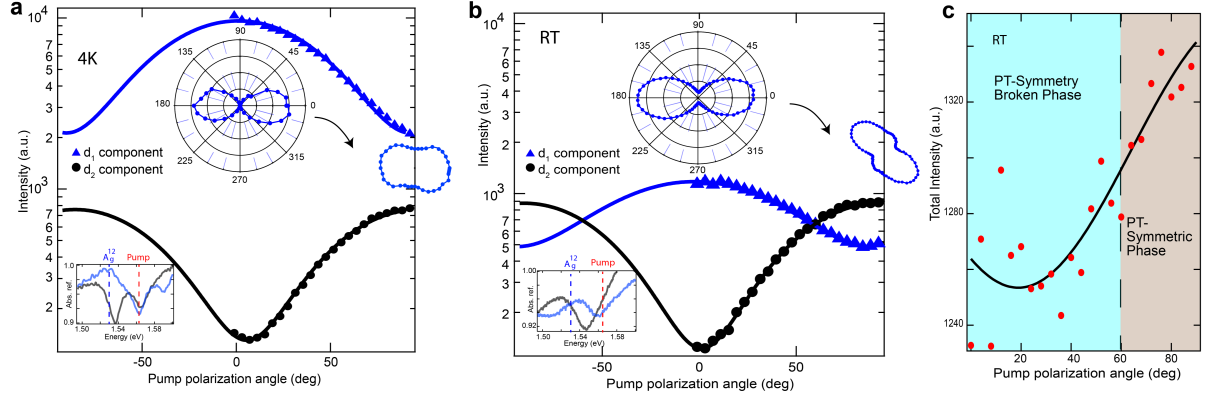


Fig. 3. Pump polarization dependence of the d_1 and d_2 components of A_g^{12} mode intensity at a. 4K and b. room temperature (RT), shown in logarithmic scale. (Middle and right insets) Polar plots showing A_g^{12} mode intensity with analyzer angle w.r.t. b-axis, for d_1 and d_2 polarized pump. Solid curves are obtained from the microscopic theory. Bottom-left inset plots indicate the relative position of the pump and emission energies with the cavity modes at 4K and RT. c. Pump polarization dependence of total intensity variation revealing a PT symmetric phase transition.

We propose two states $|\psi_j(\epsilon, k)\rangle$ ($j = 1, 2$) in polarization space of the Stokes modes forming the basis of a non-Hermitian PT-symmetric system. The Hamiltonian of two state systems can be written in the non-Hermitian form:

$$H = (|\psi_1\rangle, |\psi_2\rangle) \begin{pmatrix} \epsilon + i\delta_1 & g \\ g & \epsilon + i\delta_2 \end{pmatrix} \begin{pmatrix} |\psi_1\rangle \\ |\psi_2\rangle \end{pmatrix} \dots \dots \dots (1)$$

The real part ϵ of the diagonal elements are the energies, while the positive imaginary parts signify the gain due to stimulated Raman scattering of the coherent pump beam. Here, g is the coupling arising from the off-diagonal Raman gain tensor elements. The eigenvalues of this Hamiltonian are $E^\pm = \epsilon + i\hbar\xi_{1,2}$, where $\hbar\xi_{1,2} = \frac{\delta_1 + \delta_2}{2} \pm \sqrt{\left(\frac{\delta_1 - \delta_2}{2}\right)^2 - g^2}$. In the experiment we measure the intensity of two polarization states $|d_1\rangle$ and $|d_2\rangle$ which are the eigenstates of the above Hamiltonian. A microscopic theory has been developed (see Note S3 in the Supplemental Material and references [51,52] therein) considering the stimulated Raman processes in this anisotropic material to directly obtain the imaginary part of the eigenvalues of (1):

$$\xi_j = F_j [g_{jj} Q_j I_0 \cos(\phi_j - \theta)^2 + g_{kj} Q_k I_0 \cos(\phi_k - \theta)^2 - (g_{jj} + g_{jk}) f(T)]$$

where, j and k correspond to the indices 1, 2. F_j is the Purcell factor for the j^{th} mode at Stokes frequency, Q_j is the amplification factor for the pump, g_{jj} and g_{kj} are the diagonal and off-diagonal elements of Raman gain tensor of the material, and $f(T) = \frac{1 - \exp(-\frac{\hbar\omega}{2kT})}{\exp(\frac{\hbar\omega}{kT}) - 1}$ where, ω is the angular frequency of the phonon mode. From our experimental setup and sample orientation we find $\phi_1 =$

0° , and $\phi_2 = 80^\circ$. For a particular choice of basis states, $|\psi_j\rangle = \sum_{k=1}^2 C_k |d_k\rangle$ one can obtain the parameters g , δ_1 and δ_2 from the above expression of ξ_1 and ξ_2 . We estimated the values of Purcell factors $F_1 = 53$ and $F_2 = 1.6$ from the quality factors and detuning of the cavity for mode 1 and 2 respectively. Considering the loss of the cavity photon we apply the steady state condition in the rate equation model to obtain the expression of measured intensity (see Note S3 in the Supplemental Material). It enabled us to match our experimental data at 4 K quite satisfactorily as shown in Fig. 3a and to obtain the ratios among the four Raman gain tensor elements as fitting parameters (see Table S1). With this theoretical model we can now understand how the single mode selectivity in this PT-symmetric system is giving rise to the zero-threshold laser, as follows. Single mode ($|d_1\rangle$) amplification and a simultaneous abatement of the other mode ($|d_2\rangle$), requires two eigenvalues $E^+ = \epsilon + i\hbar\xi_1$, and $E^- = \epsilon + i\hbar\xi_2$. A larger difference between ξ_1 and ξ_2 ensures a highly polarized single mode laser which happens in the PT-symmetry broken phase with $\xi_1 \gg \xi_2$. Experimentally, this regime is best achieved at lower temperature as shown in Fig. S4 (see Supplemental Material), when the system is pumped with d_1 polarization. By incorporating the spectral overlap factor β in our microscopic model, we find the experimentally obtained linear power dependence for zero threshold when $\beta = 1$ (see Note S3(b) in the Supplemental Material and references [53–58] therein).

According to our model, when the pump beam is d_2 polarized, the system is still in the PT-symmetry broken phase but the inequality $\xi_1 > \xi_2$ become relatively weaker resulting in unpolarized emission of the two Stokes modes. Importantly, the validity of our model is verified by predicting the data at 300 K quite accurately as shown in Fig. 3b where similar ratio of Raman gain tensor elements g_{jj}, g_{kj} obtained at 4 K have been utilized with suitable modification of the Purcell factors as the cavity is detuned. Interestingly, we observe that at $T = 300 K$, the system can reach to the PT-symmetric condition at particular $\theta = 60^\circ$ When $\xi_1 = \xi_2$ which corresponds to the crossing of intensities of the d_1 and d_2 components as seen in Fig. 3b. To better understand the phase transition at room temperature, we plot the total intensity variation with respect to pump polarization. Initially, the total intensity decreases as the gain contrast reduces; however, intriguingly, the trend reverses after $\theta = 20^\circ$. The experimental data is comparable with the theory as illustrated in Fig 3c. This non-trivial phenomenon is analogous to loss-induced transparency [15] reported in passive PT-symmetric systems [15]. From the power dependence data at various temperatures, we observe the characteristic power dependence of zero-threshold lasing persisting up to 100 K, after that the intensity reduces drastically as shown in Fig. S4 (see Supplemental Material).

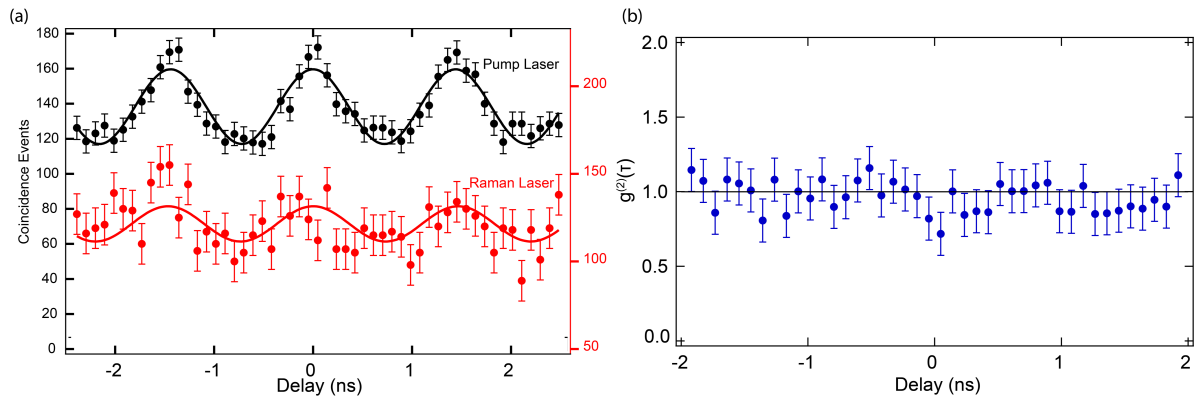


Fig. 4: Results of second-order correlation measurements. **a.** Coincidence events recorded using a Hanbury-Brown-Twiss (HBT) setup to measure second-order correlation, for the pump laser (black circles) and the emission from A_g^{12} (red circles) at high pump power. The solid red and black lines are the best fits obtained using the model $g^{(2)}(\tau) = A + B \cos(2\Delta\omega\tau)$. The error bars indicate the uncertainty due to Poisson distribution statistics. **b.** Second order correlation $g^{(2)}(\tau)$ of the A_g^{12} Raman mode (with d_1 polarized pump,

which corresponds to the zero-threshold laser condition) obtained by normalizing with respect to the pump laser's $g^{(2)}(\tau)$. The error bars indicate the uncertainty due to Poisson distribution statistics.

Apart from the power dependence and degree of polarization of the zero-threshold Raman laser we measured the second-order correlation to provide further support of its coherence characteristic. At higher pump power with d_1 polarization we selected the Stokes mode with the strongest emission, A_g^{12} for the $g^{(2)}$ measurement. We first characterized the CW pump laser itself and found a slight sinusoidal modulation in $g^{(2)}$ (see Fig 4a) due to the superposition of frequencies $\omega_0 \pm \Delta\omega$ present within the linewidth of the pump laser with central frequency ω_0 . $\Delta\omega$ was obtained as ~ 2 GHz (see Methods in Supplemental Material) with the data shown in Fig 4a. After characterizing the $g^{(2)}$ of the pump beam, we measured the $g^{(2)}$ for A_g^{12} mode at >6 mW pump power. Figure 4a shows the result of $g^{(2)}$ measurements, where we do not observe the peak in $g^{(2)}$ at zero time delay ($\tau = 0$) expected for spontaneous emission. Instead, $g^{(2)}(\tau)$ retains the variation of the pump beam, which provides further proof of coherence of the emitted Raman laser signal. After normalizing with the $g^{(2)}$ of the pump laser, we obtain a flat $g^{(2)}$ which is the signature of a laser as shown in Fig 4b.

All the lasing modes that have been discussed are directional, with different angles of emission for each of the Raman modes satisfying the resonance condition with each of the polariton branches at different in-plane momenta, as shown in the angle resolved measurement in Fig. S7 (see Supplemental Material). The robustness of zero threshold lasing and reproducibility of all the experimental results as discussed above has been observed in a different ReS₂ flake of similar thickness inside the same cavity, kept at the same orientation as the previous one, which is shown in Fig. S8 (see Supplemental Material).

Conclusions

We demonstrated a zero threshold Raman laser in a system of anisotropic microcavity exciton-polaritons and proposed a theory to describe a two-state system comprised of polarized Stokes mode inside microcavity as a non-Hermitian PT-symmetric system. A quantum mechanical time evolution of the proposed loss-gain system successfully explains our observation of highly polarized zero-threshold lasing. Importantly, a microscopic theory of stimulated resonant Raman scattering of anisotropic material enabled us to estimate the parameters of the proposed Hamiltonian. We expect that the threshold less lasing action demonstrated in our system is quite generic and could be observed in any single mode microcavity hosting anisotropic Raman active materials supporting polarized excitons. We believe our proposed theory of zero-threshold Raman laser presented in this work can open up a broader application involving anisotropic materials in optical microcavity, such as, it can be applicable to various nonlinear and parametric processes which are in resonance with the microcavity. Thus, it can pave the way to a new research direction in quantum science and technology involving non-Hermitian PT-symmetry, but also offers a significant advance in threshold less micro-lasers, and quantum frequency converters with numerous applications in quantum optics and information.

Acknowledgements:

We thank Prof. S. P. Khastgir and Prof. G. S. Agarwal and Prof. Jyotirmoy Bhattacharya for valuable discussions on this work. This work has been supported by funding from the Science and Engineering Research Board (CRG/2018/002845, CRG/2021/000811); Ministry of Education (MoE/STARS- 1/647); Council of Scientific and Industrial Research, India (09/081(1352)/2019-EMR-I); Department of Science and Technology, Ministry of Science and Technology, India (IF180046) and Indian Institute of Technology Kharagpur.

Author contributions:

SD conceptualized the project. AD, DC, KG, ARC and SD contributed in the sample fabrication. AD, DC, PD and SD formulated the experiments, performed data analysis. PD, DC and SD developed the theory. AD, DC, PD performed all optical measurements. AD, DC, PD and SD drafted the paper, and all authors contributed to reviewing and editing the final draft. SD supervised the project.

References

- [1] S. M. Spillane, T. J. Kippenberg, and K. J. Vahala, Ultralow-threshold Raman laser using a spherical dielectric microcavity, *Nature* **415**, 6872 (2002).
- [2] I. S. Grudin and L. Maleki, Ultralow-threshold Raman lasing with CaF_2 resonators, *Opt. Lett.*, **OL 32**, 166 (2007).
- [3] Y. Takahashi, Y. Inui, M. Chihara, T. Asano, R. Terawaki, and S. Noda, A micrometre-scale Raman silicon laser with a microwatt threshold, *Nature* **498**, 7455 (2013).
- [4] R. Tyumenev, J. Hammer, N. Y. Joly, P. St. J. Russell, and D. Novoa, Tunable and state-preserving frequency conversion of single photons in hydrogen, *Science* **376**, 621 (2022).
- [5] W. Gao, X. Li, M. Bamba, and J. Kono, Continuous transition between weak and ultrastrong coupling through exceptional points in carbon nanotube microcavity exciton–polaritons, *Nature Photonics* **12**, 6 (2018).
- [6] T. Gao et al., Observation of non-Hermitian degeneracies in a chaotic exciton-polariton billiard, *Nature* **526**, 7574 (2015).
- [7] D. Chakrabarty, A. Dhara, P. Das, K. Ghosh, A. R. Chaudhuri, and S. Dhara, *Anisotropic Exciton Polariton Pairs as a Platform for PT-Symmetric Non-Hermitian Physics*, arXiv:2305.17472.
- [8] J. Yuen-Zhou, S. K. Saikin, T. Zhu, M. C. Onbasli, C. A. Ross, V. Bulovic, and M. A. Baldo, Plexciton Dirac points and topological modes, *Nat Commun* **7**, 11783 (2016).
- [9] H. G. Song, M. Choi, K. Y. Woo, C. H. Park, and Y.-H. Cho, Room-temperature polaritonic non-Hermitian system with single microcavity, *Nat. Photon.* **15**, 8 (2021).
- [10] R. Su, E. Estrecho, D. Biegańska, Y. Huang, M. Wurdack, M. Pieczarka, A. G. Truscott, T. C. H. Liew, E. A. Ostrovskaya, and Q. Xiong, Direct measurement of a non-Hermitian topological invariant in a hybrid light-matter system, *Science Advances* **7**, eabj8905 (2021).
- [11] E. J. Bergholtz, J. C. Budich, and F. K. Kunst, Exceptional topology of non-Hermitian systems, *Rev. Mod. Phys.* **93**, 015005 (2021).
- [12] Y. Li, X. Ma, Z. Hatzopoulos, P. G. Savvidis, S. Schumacher, and T. Gao, Switching Off a Microcavity Polariton Condensate near the Exceptional Point, *ACS Photonics* **9**, 2079 (2022).
- [13] L. Feng, Z. J. Wong, R.-M. Ma, Y. Wang, and X. Zhang, Single-mode laser by parity-time symmetry breaking, *Science* **346**, 972 (2014).
- [14] H. Hodaei, M.-A. Miri, M. Heinrich, D. N. Christodoulides, and M. Khajavikhan, Parity-time–symmetric microring lasers, *Science* **346**, 975 (2014).
- [15] A. Guo, G. J. Salamo, D. Duchesne, R. Morandotti, M. Volatier-Ravat, V. Aimez, G. A. Siviloglou, and D. N. Christodoulides, Observation of P T -Symmetry Breaking in Complex Optical Potentials, *Phys. Rev. Lett.* **103**, 093902 (2009).
- [16] C. E. Rüter, K. G. Makris, R. El-Ganainy, D. N. Christodoulides, M. Segev, and D. Kip, Observation of parity–time symmetry in optics, *Nature Phys* **6**, 3 (2010).

- [17] B. Peng, Ş. K. Özdemir, M. Liertzer, W. Chen, J. Kramer, H. Yilmaz, J. Wiersig, S. Rotter, and L. Yang, Chiral modes and directional lasing at exceptional points, *Proceedings of the National Academy of Sciences* **113**, 6845 (2016).
- [18] K. V. Kepesidis, T. J. Milburn, J. Huber, K. G. Makris, S. Rotter, and P. Rabl, \mathcal{P} -symmetry breaking in the steady state of microscopic gain–loss systems, *New J. Phys.* **18**, 095003 (2016).
- [19] L. Zhang, G. S. Agarwal, W. P. Schleich, and M. O. Scully, Hidden \mathcal{PT} symmetry and quantization of a coupled-oscillator model of quantum amplification by superradiant emission of radiation, *Phys. Rev. A* **96**, 013827 (2017).
- [20] L. Feng, R. El-Ganainy, and L. Ge, Non-Hermitian photonics based on parity–time symmetry, *Nature Photon* **11**, 12 (2017).
- [21] R. El-Ganainy, K. G. Makris, M. Khajavikhan, Z. H. Musslimani, S. Rotter, and D. N. Christodoulides, Non-Hermitian physics and \mathcal{PT} symmetry, *Nature Phys* **14**, 1 (2018).
- [22] S. Wu et al., Monolayer semiconductor nanocavity lasers with ultralow thresholds, *Nature* **520**, 7545 (2015).
- [23] Y. Ye, Z. J. Wong, X. Lu, X. Ni, H. Zhu, X. Chen, Y. Wang, and X. Zhang, Monolayer excitonic laser, *Nature Photon* **9**, 11 (2015).
- [24] J. Shang et al., Room-temperature 2D semiconductor activated vertical-cavity surface-emitting lasers, *Nat Commun* **8**, 1 (2017).
- [25] X. Liu, T. Galfsky, Z. Sun, F. Xia, E. Lin, Y.-H. Lee, S. Kéna-Cohen, and V. M. Menon, Strong light–matter coupling in two-dimensional atomic crystals, *Nature Photon* **9**, 1 (2015).
- [26] S. Dhara, C. Chakraborty, K. M. Goodfellow, L. Qiu, T. A. O’Loughlin, G. W. Wicks, S. Bhattacharjee, and A. N. Vamivakas, Anomalous dispersion of microcavity trion-polaritons, *Nature Phys* **14**, 130 (2018).
- [27] O. B. Aslan, D. A. Chenet, A. M. van der Zande, J. C. Hone, and T. F. Heinz, Linearly Polarized Excitons in Single- and Few-Layer ReS_2 Crystals, *ACS Photonics* **3**, 96 (2016).
- [28] A. Dhara, D. Chakraborty, P. Das, A. K. Pattanayak, S. Paul, S. Mukherjee, and S. Dhara, Additional excitonic features and momentum-dark states in ReS_2 , *Phys. Rev. B* **102**, 161404 (2020).
- [29] D. Chakraborty, A. Dhara, K. Ghosh, A. K. Pattanayak, S. Mukherjee, A. R. Chaudhuri, and S. Dhara, Interfacial anisotropic exciton-polariton manifolds in ReS_2 , *Optica*, *OPTICA* **8**, 1488 (2021).
- [30] B. Peng, Ş. K. Özdemir, F. Lei, F. Monifi, M. Gianfreda, G. L. Long, S. Fan, F. Nori, C. M. Bender, and L. Yang, Parity–time-symmetric whispering-gallery microcavities, *Nature Phys* **10**, 5 (2014).
- [31] L. Chang, X. Jiang, S. Hua, C. Yang, J. Wen, L. Jiang, G. Li, G. Wang, and M. Xiao, Parity–time symmetry and variable optical isolation in active–passive-coupled microresonators, *Nature Photon* **8**, 7 (2014).
- [32] S. Richter, T. Michalsky, C. Sturm, B. Rosenow, M. Grundmann, and R. Schmidt-Grund, Exceptional points in anisotropic planar microcavities, *Phys. Rev. A* **95**, 023836 (2017).
- [33] T. Gao et al., Chiral Modes at Exceptional Points in Exciton-Polariton Quantum Fluids, *Phys. Rev. Lett.* **120**, 065301 (2018).
- [34] J. Zhang, B. Peng, Ş. K. Özdemir, K. Pichler, D. O. Krimer, G. Zhao, F. Nori, Y. Liu, S. Rotter, and L. Yang, A phonon laser operating at an exceptional point, *Nature Photon* **12**, 8 (2018).
- [35] M. Kremer, T. Biesenthal, L. J. Maczewsky, M. Heinrich, R. Thomale, and A. Szameit, Demonstration of a two-dimensional \mathcal{PT} -symmetric crystal, *Nat Commun* **10**, 1 (2019).
- [36] M.-A. Miri and A. Alù, Exceptional points in optics and photonics, *Science* **363**, eaar7709 (2019).
- [37] Ş. K. Özdemir, S. Rotter, F. Nori, and L. Yang, Parity–time symmetry and exceptional points in photonics, *Nat. Mater.* **18**, 8 (2019).
- [38] J. B. Khurgin, Exceptional points in polaritonic cavities and subthreshold Fabry–Perot lasers, *Optica*, *OPTICA* **7**, 1015 (2020).

- [39] A. McCreary, J. R. Simpson, Y. Wang, D. Rhodes, K. Fujisawa, L. Balicas, M. Dubey, V. H. Crespi, M. Terrones, and A. R. Hight Walker, Intricate Resonant Raman Response in Anisotropic ReS₂, *Nano Lett.* **17**, 5897 (2017).
- [40] J. Jadczak, J. Kutrowska-Girzycka, T. Smoleński, P. Kossacki, Y. S. Huang, and L. Bryja, Exciton binding energy and hydrogenic Rydberg series in layered ReS₂, *Sci Rep* **9**, 1578 (2019).
- [41] A. Fainstein, B. Jusserand, and V. Thierry-Mieg, Raman Scattering Enhancement by Optical Confinement in a Semiconductor Planar Microcavity, *Phys. Rev. Lett.* **75**, 3764 (1995).
- [42] A. Fainstein, B. Jusserand, and V. Thierry-Mieg, Cavity-Polariton Mediated Resonant Raman Scattering, *Phys. Rev. Lett.* **78**, 1576 (1997).
- [43] A. K. Pattanayak, P. Das, A. Dhara, D. Chakrabarty, S. Paul, K. Gurnani, M. M. Brundavanam, and S. Dhara, A Steady-State Approach for Studying Valley Relaxation Using an Optical Vortex Beam, *Nano Lett.* **22**, 4712 (2022).
- [44] Y. Zhou et al., Stacking-Order-Driven Optical Properties and Carrier Dynamics in ReS₂, *Adv. Mater.* **32**, 1908311 (2020).
- [45] J. McKeever, A. Boca, A. D. Boozer, J. R. Buck, and H. J. Kimble, Experimental realization of a one-atom laser in the regime of strong coupling, *Nature* **425**, 6955 (2003).
- [46] Y. Yamamoto and R. E. Slusher, Optical Processes in Microcavities, *Physics Today* **46**, 66 (1993).
- [47] M. Khajavikhan, A. Simic, M. Katz, J. H. Lee, B. Slutsky, A. Mizrahi, V. Lomakin, and Y. Fainman, Thresholdless nanoscale coaxial lasers, *Nature* **482**, 7384 (2012).
- [48] I. Prieto, J. M. Llorens, L. E. Muñoz-Camúñez, A. G. Taboada, J. Canet-Ferrer, J. M. Ripalda, C. Robles, G. Muñoz-Matutano, J. P. Martínez-Pastor, and P. A. Postigo, Near thresholdless laser operation at room temperature, *Optica*, *OPTICA* **2**, 66 (2015).
- [49] K. Wu, Y.-S. Park, J. Lim, and V. I. Klimov, Towards zero-threshold optical gain using charged semiconductor quantum dots, *Nature Nanotech* **12**, 12 (2017).
- [50] S. T. Jagsch et al., A quantum optical study of thresholdless lasing features in high- β nitride nanobeam cavities, *Nat Commun* **9**, 1 (2018).
- [51] A. Yariv, *Quantum Electronics*, 3rd ed (Wiley, New York, 1989).
- [52] Y. Wu, X. Yang, and P. T. Leung, Theory of microcavity-enhanced Raman gain, *Opt. Lett.*, *OL* **24**, 345 (1999).
- [53] H. Yokoyama and S. D. Brorson, Rate equation analysis of microcavity lasers, *Journal of Applied Physics* **66**, 4801 (1989).
- [54] X. Checoury, Z. Han, M. El Kurdi, and P. Boucaud, Deterministic measurement of the Purcell factor in microcavities through Raman emission, *Phys. Rev. A* **81**, 033832 (2010).
- [55] G. Bjork and Y. Yamamoto, Analysis of semiconductor microcavity lasers using rate equations, *IEEE J. Quantum Electron.* **27**, 2386 (1991).
- [56] B. Petrak, N. Djeu, and A. Muller, Purcell-enhanced Raman scattering from atmospheric gases in a high-finesse microcavity, *Phys. Rev. A* **89**, 023811 (2014).
- [57] A. V. Kavokin, J. Baumberg, G. Malpuech, and F. P. Laussy, *Microcavities*, Second edition (Oxford University Press, Oxford, 2017).
- [58] J. B. Khurgin and M. A. Noginov, How Do the Purcell Factor, the Q-Factor, and the Beta Factor Affect the Laser Threshold?, *Laser & Photonics Reviews* **15**, 2000250 (2021).

Supplemental Material for

A Zero-Threshold PT-Symmetric Polariton-Raman Laser

Avijit Dhara^{1†}, Pritam Das^{1†}, Devarshi Chakrabarty^{1†}, Kritika Ghosh², Ayan Roy Chaudhuri², Sajal Dhara^{1*}

¹*Department of Physics, IIT Kharagpur, Kharagpur-721302, India*

²*Materials Science Centre, IIT Kharagpur, Kharagpur-721302, India*

[†] *These authors contributed equally*

^{*} *Corresponding author. email: sajal dhara@phy.iitkgp.ac.in*

List of Contents:

Notes S1-S4

Figs. S1-S11

References

Note S1. Methods

Sample fabrication

We prepared three samples of ReS₂ with the same thickness: two embedded in a microcavity and the other stacked on SiO₂/Si (henceforth also referred to as a ‘bare’ sample). The microcavity consists of two distributed Bragg reflectors (DBRs). The bottom mirror comprises 10 pairs of SiO₂/Ta₂O₅ films, grown using the RF sputtering technique. Two ReS₂ crystal of thickness 10 nm are exfoliated by the dry transfer method and transferred on the bottom mirror. The top DBR of 8 pairs of SiO₂/Ta₂O₅ is then deposited using the same sputtering method. The other sample is prepared by dry transfer of exfoliated 10 nm thick ReS₂ crystal on the Si/SiO₂ substrate. We estimate the sample thickness from optical contrast. Sample image is shown in Fig. S5.

Measurement

All optical measurements were performed with the sample placed in a closed cycle microscopy cryostat (Montana Instruments) with a variable temperature range of 3.2 to 295 K. For the Raman study, we excite the sample using backscattering geometry with a Ti: Sapphire laser (Coherent—MIRA) in CW mode with a pump energy of 1.564 eV ($\lambda_{excitation} = 792.8$ nm). The excitation path contains a linear polarizer followed by a half-wave plate mounted on a motorized rotational stage to control the polarization of the pump beam. Polarization state of light beam was preserved throughout the optical path via a special design in our optical setup as discussed elsewhere [1] for polarization resolved Raman spectroscopy. The laser beam was focused to a spot size ~ 1 μ m by a 60X objective lens with numerical aperture of 0.7. The Raman stokes signal is collected through the same objective lens and dispersed by a diffraction grating with 1200 grooves per mm and detected by a nitrogen-cooled CCD (Pylon 400) with spectral resolution of 0.5 cm^{-1} . In the temperature dependent power variation study, to attenuate scattered light of the laser from the optical elements in the beam path and increase the signal-to-noise ratio, an analyzer is kept before the spectrometer, crossed with the laser polarization. A broadband light source (Thorlabs SLS202L) is used for reflectance measurements.

Anisotropic polariton dispersion and cavity parameters

The polariton dispersions can be obtained by diagonalizing the following Hamiltonian:

$$H = \hbar\omega_i(k)C_{ik}^\dagger C_{ik} + \hbar\omega_j X_{jk}^\dagger X_{jk} + v_j \hat{e}_i \cdot \hat{d}_j [C_{ik}^\dagger X_{jk} + X_{jk}^\dagger C_{ik}]$$

Here, C_{ik} , X_{jk} are the annihilation operators in the in-plane momentum (k) space for the photonic and excitonic modes respectively, \hat{e}_i is the in-plane polarization unit vector of the photonic modes. Indices i and j labels the TE, TM, and two anisotropic excitons X_1 , X_2 respectively. The non-Hermitian Hamiltonian given above has a set of exceptional points (EPs), or degeneracies in the polariton eigenmodes, observed at specific points in the parameter space of polarization and in-plane wavevector. A systematic study of these EPs has been presented in a related study. [2]

By fitting the 4x4 coupled oscillator model, we found the maximum value of the coupling strengths v_1 and v_2 to be 14.5 and 18.6 meV respectively at 4 K. The coupling strengths can be tuned by rotating the pump polarization, and the system can be tuned from the strong to weak coupling regime. The Q factor for the composite cavity consisting of SiO₂ and ReS₂ is ~ 300 .

Second order correlation measurements

To measure the $g^{(2)}$ correlation of the Raman emission from the microcavity, we have used single photon detectors from IDQ, with a timing resolution (FWHM) of 40 ps, and TCSPC module of time resolution 2 ps from Becker & Hickl (SPC-130IN). We filtered out the specific Raman signal using a monochromator with spectral resolution of 0.9 Å. After carefully aligning our HBT interferometer, we characterize the $g^{(2)}$ of the pump obtained in pulsed (ps) and CW mode from our tunable Ti-Sapphire laser reflected from the microcavity, as shown in Fig S11. In pulsed mode, there is a separation of 13.2 ns between the pulses, which matches well with the repetition rate of the laser which is 76 MHz.

The variation in $g^{(2)}(\tau)$ for the pump laser is modelled as follows. For a given amplitude $E = E_0 \cos\omega_0 t + E_1 [\cos(\omega_0 + \Delta\omega)t + \cos(\omega_0 - \Delta\omega)t]$, we can evaluate $g^{(2)}(\tau)$ as $A + B \cos(2\Delta\omega\tau) + C \cos(\omega_0\tau)$. Due to the finite time resolution (40 ps) of the photodetectors, the term $C \cos(\omega_0\tau)$ with corresponding time period ~ 3 attoseconds has no contribution to the experimental observation. Thus, we only observe $g^{(2)}(\tau) = A + B \cos(2\Delta\omega\tau)$.

Due to the limited strength of the Raman signal reaching the photodetector (corresponding to a count rate of 13,000 photons/second), we had chosen a bin size of 96 ps in order to build reasonable statistics over 32 hours.

Note S2. Stacking order in ReS₂

We identify several Raman modes which exactly match with existing literature, such as: A_g^4 (139 cm^{-1}), A_g^5 (144 cm^{-1}), A_g^1 (152 cm^{-1}), A_g^7 (214 cm^{-1}), A_g^8 (236 cm^{-1}), A_g^9 (276 cm^{-1}), A_g^{10} (284 cm^{-1}), A_g^{12} (311 cm^{-1}), A_g^{13} (320 cm^{-1}), A_g^{14} (325 cm^{-1}), A_g^{15} (349 cm^{-1}), A_g^{16} (369 cm^{-1}), A_g^{17} (378 cm^{-1}), A_g^{18} (408 cm^{-1}), A_g^3 (420 cm^{-1}) and A_g^2 (440 cm^{-1}), shown in Fig. S6.

Recently, it has been reported that ReS₂ crystal has two stable stacking orders (AA and AB) [4], which have been identified by the separation between the A_g^4 and A_g^1 modes. The separation between these two modes in both cases (inside microcavity and bare sample) is 13 cm^{-1} , as found in AA stacking ReS₂ crystal, as shown in Fig. S1.

Note S3. Microscopic theory for stimulated Raman scattering in anisotropic microcavity

To derive the microscopic model for Raman scattering, we consider the vibrational states of the ground electronic state of ReS₂. We use a two-dimensional model, in which the potential landscape of this state can be approximated as a displaced harmonic potential. The induced polarization density of ReS₂ can be written as [5]:

$$P_j = \varepsilon_0 \chi_{jk} E_k = \varepsilon_0 \left((\chi_{jk})_0 + \left(\frac{\partial \chi_{jk}}{\partial q_1} \right)_0 q_1 + \left(\frac{\partial \chi_{jk}}{\partial q_2} \right)_0 q_2 \right) E_k \dots \dots \dots (2)$$

Here, q_1, q_2 are the two normal coordinates of vibration associated with the two polarized Stokes emissions. $(\chi_{jk})_0$ is the susceptibility tensor element in the equilibrium position. E_k is the electric field component.

Therefore, from (2) the interaction Hamiltonian density contributing to the Raman process can be expressed as follows:

$$\begin{aligned} H_{int} &= - \sum_{j=1}^2 P_j E_j = - \sum_{j=1}^2 \sum_{k=1}^2 \varepsilon_0 \left(\left(\frac{\partial \chi_{jk}}{\partial q_1} \right)_0 q_1 + \left(\frac{\partial \chi_{jk}}{\partial q_2} \right)_0 q_2 \right) E_k E_j \\ &= - \sum_{j=1}^2 \sum_{k=1}^2 \sum_{\mu=1}^2 \varepsilon_0 R_{jk\mu} q_\mu E_k E_j \dots \dots \dots (3) \end{aligned}$$

Where $R_{jk\mu} = \left(\frac{\partial \chi_{jk}}{\partial q_\mu} \right)$ is the Raman tensor element. To capture the effect of stimulated Raman scattering, we consider the system has been excited in the presence of both pump and Stokes frequencies with d_1 and d_2 polarization. i.e.

$$E_j(t) = E_{lj} \cos \omega_l t + E_{sj} \cos \omega_s t$$

Where $j = 1$ and 2 indicate d_1 and d_2 polarizations of the electric field.

Quantized electric fields inside microcavity can be expressed using creation and annihilation operators corresponding to the pump and Stokes photons, denoted as (a_{lj}^+, a_{lj}) and (a_{sj}^+, a_{sj}) . Here, the index j indicates the polarization mode, as mentioned previously.

The operator \hat{E}_j can be expressed in terms of the photon creation and annihilation operators:

$$\hat{E}_j = \hat{E}_{lj} + \hat{E}_{sj} = \left[i \sqrt{\frac{\hbar \omega_l}{2 \varepsilon_0 V_{eff}}} (a_{lj}^+ - a_{lj}) + i \sqrt{\frac{\hbar \omega_s}{2 \varepsilon_0 V_{eff}}} (a_{sj}^+ - a_{sj}) \right]$$

In the harmonic potential approximation, the vibrational levels separated by phonon frequency ν can be quantized using the phonon creation and annihilation operators b_j^+ and b_j . We can now define the normal coordinate as $\hat{q}_j = q_0 (b_j^+ + b_j)$ where, q_0 is zero-point amplitude of vibration. Here, the index $j = 1$ and 2 indicate normal coordinate of vibration in two orthogonal directions.

The Hamiltonian density of the system can be written as,

$$H = H_0 + H_{int}$$

Where, H_0 is the unperturbed Hamiltonian density:

$$H_0 = \sum_{j=1}^2 \left[\hbar \omega_l \left(a_{lj}^+ a_{lj} + \frac{1}{2} \right) + \hbar \omega_s \left(a_{sj}^+ a_{sj} + \frac{1}{2} \right) + \hbar \nu \left(b_j^+ b_j + \frac{1}{2} \right) \right]$$

The interaction Hamiltonian density given in Eqn. (3) can be written as:

$$H_{int} = - \sum_{j=1}^2 \sum_{k=1}^2 \sum_{\mu=1}^2 [\varepsilon_0 R_{jk\mu} \hat{q}_\mu \hat{E}_j \hat{E}_k]$$

We consider the non-zero contributions of the Raman processes involving emission and absorption of polarized Stokes photons due to interaction with co-polarized and cross-polarized pump photons are denoted by H_{int}^{co} and H_{int}^{cross} respectively. These processes are illustrated in Fig. S9.

Therefore, the interaction Hamiltonian density is reduced to $H_{int} = H_{int}^{co} + H_{int}^{cross}$, where:

$$H_{int}^{co} = - \sum_{j=1}^2 [\varepsilon_0 R_{jjj} \hat{Q}_j \hat{E}_{lj} \hat{E}_{sj}]$$

$$H_{int}^{cross} = - \sum_{j=1}^2 \sum_{\{j \neq k, k=1\}}^2 [\varepsilon_0 R_{jkk} \hat{Q}_k \hat{E}_{lj} \hat{E}_{sk}]$$

After substituting the expression of \hat{E}_{lj} , \hat{E}_{sj} , and \hat{Q}_j , the non-zero terms contributing to the Raman processes can be written as:

$$H_{int}^{co} = -\hbar\Omega \sum_{j=1}^2 R_{jjj} [(a_{lj} a_{sj}^+ b_j^+) + (h.c.)], \text{ and } H_{int}^{cross} = -\hbar\Omega \sum_{j=1}^2 \sum_{\{j \neq k, k=1\}}^2 R_{jkk} [(a_{lj} a_{sk}^+ b_k^+) + (h.c.)]$$

Where $\Omega = \frac{q_0 \sqrt{\omega_s \omega_l}}{V_{eff}}$. The composite state of the system is constructed from the tensor product of the pump, Stokes photons, and phonon number states, represented as $|n_{l1}, n_{l2}, n_{s1}, n_{s2}, n_1, n_2\rangle$. Here, n_{lj}, n_{sj}, n_j denote the photon numbers of the pump, Stokes modes and phonon number respectively, with index $j = 1, 2$ implying d_1, d_2 polarization of photons and excited phonon modes corresponding to two polarized Stokes emissions.

We use Bose-Einstein statistics for phonon occupation number in ground and 1st excited state of vibrational energy level denoted as P_a and P_b respectively. The transition rate for emission of j^{th} -Stokes photons via annihilation of co and cross polarized pump photons are denoted by Γ_{jj} and Γ_{kj} respectively.

Consequently, Total emission rate for j^{th} -Stokes photons:

$$\Gamma = \Gamma_{jj} + \Gamma_{kj}$$

$$\Gamma_{jj} = \frac{2\pi}{\hbar^2} V_{eff}^2 P_a |\langle n_{lj} - 1, n_{sj} + 1, n_{lk}, n_{sk}, \delta_{1j}, \delta_{2j} | \hbar\Omega R_{jjj} (a_{lj} a_{sj}^+ b_j^+) | n_{lj}, n_{sj}, n_{lk}, n_{sk}, 0, 0 \rangle|^2 \rho_c(\omega_s)$$

$$= \left[\frac{2\pi}{\hbar^2} (\hbar\Omega V_{eff})^2 \rho_0 \right] R_{jjj} P_a n_{lj} (n_{sj} + 1) F_j$$

$$= \alpha_{jj} P_a n_{lj} (n_{sj} + 1) F_j$$

$$\Gamma_{kj} = \frac{2\pi}{\hbar^2} V_{eff}^2 P_a |\langle n_{lj}, n_{sj} + 1, n_{lk} - 1, n_{sk}, \delta_{2j}, \delta_{1j} | \hbar\Omega R_{kjj} (a_{lk} a_{sj}^+ b_j^+) | n_{lj}, n_{sj}, n_{lk}, n_{sk}, 0, 0 \rangle|^2 \rho_c(\omega_s)$$

$$= \left[\frac{2\pi}{\hbar^2} (\hbar\Omega V_{eff})^2 \rho_0 \right] R_{kjj} P_a n_{lk} (n_{sj} + 1) F_j$$

$$= \alpha_{kj} P_a n_{lk} (n_{sj} + 1) F_j$$

Here, δ_{1j}, δ_{2j} are the Kronecker delta and $\alpha_{kj} = R_{kjj} \left[\frac{2\pi}{\hbar^2} (\hbar\Omega V_{eff})^2 \rho_0 \right]$ is Raman tensor element of bulk ReS₂ multiplied with a constant. F_j is the Purcell factor corresponding to the d_j -polarized polariton mode by which the vacuum photon density $\rho_0(\omega_s)$ is enhanced inside the microcavity [6].

Similarly, the rates of the inverse processes, where a pump photon is emitted while a co-polarized and cross polarized Stokes photon is absorbed, can be written,

$$\Gamma' = \Gamma'_{jj} + \Gamma'_{kj} = \alpha_{jj} P_b n_{sj} (n_{lj} + 1) F_j + \alpha_{kj} P_b n_{sj} (n_{lk} + 1) F_j$$

Therefore, the overall rate of change of the j^{th} -Stokes photons number can be written as:

$$\frac{dn_{sj}}{dt} = \Gamma - \Gamma' - \frac{n_{sj}}{\tau_j}$$

$$= \left[\alpha_{jj}F_j(P_a - P_b)n_{lj} + \alpha_{kj}F_j(P_a - P_b)n_{lk} - P_bF_j(\alpha_{jj} + \alpha_{kj}) - \frac{1}{\tau_j} \right] n_{sj} + P_aF_j(\alpha_{jj}n_{lj} + \alpha_{kj}n_{lk})$$

Where τ_j is the finite lifetime of Stokes photon due cavity loss. We write $\alpha_{kj}(P_a - P_b) = g_{kj}$, where g_{kj} is the stimulated Raman gain per unit intensity, and F_i is the Purcell factor corresponding to the d_i -polarized polariton mode by which the Raman gain is enhanced inside the microcavity.

The pump photon number (n_{lj}) can be controlled with a polarizer as a function of polarizer angle θ , with respect to the lab frame which can be written as follows:

$$n_{lj} = Q_j I_0 \text{Cos}(\phi_j - \theta)^2$$

Where I_0 is the intensity of pump photons inside the cavity, Q_j being the quality factor of the cavity mode resonant with the pump frequency. Here, $\phi_{j=1,2}$ is the angle of $d_{j=1,2}$ axis of the sample in the lab-frame. Thus,

$$\frac{dn_{sj}}{dt} = [F_j\{g_{jj}Q_jI_0\text{Cos}(\phi_j - \theta)^2 + g_{kj}Q_kI_0\text{Cos}(\phi_k - \theta)^2 - (g_{jj} + g_{kj})f(T)\} - \frac{1}{\tau_j}]n_{sj} + F_j(f(T) + 1) \left[(g_{jj}Q_jI_0\text{Cos}(\phi_j - \theta)^2 + g_{kj}Q_kI_0\text{Cos}(\phi_k - \theta)^2) \right] \dots\dots\dots(4)$$

Where $f(T) = \frac{1 - \exp(-\frac{\hbar\omega}{2kT})}{\exp(\frac{\hbar\omega}{kT}) - 1}$. We define ξ_j and c_j :

$$\xi_j = F_j[g_{jj}Q_jI_0\text{Cos}(\phi_j - \theta)^2 + g_{kj}Q_kI_0\text{Cos}(\phi_k - \theta)^2 - (g_{jj} + g_{kj})f(T)]$$

$$c_j = F_j(f(T) + 1) \left[(g_{jj}Q_jI_0\text{Cos}(\phi_j - \theta)^2 + g_{kj}Q_kI_0\text{Cos}(\phi_k - \theta)^2) \right]$$

Such that, the rate equation can be written as:

$$\frac{dn_{sj}}{dt} = \left[\xi_j - \frac{1}{\tau_j} \right] n_{sj} + c_j \dots\dots\dots(5)$$

We identify the coefficient ξ_j as the gain coefficient for the j^{th} Stokes modes. Due to the loss in the cavity, the overall coefficient $\left(\xi_j - \frac{1}{\tau_j} \right)$ of n_{sj} becomes negative which enables the system to reach the steady state. For steady-state condition, $\frac{dn_{sj}}{dt} = 0$. Thus, solving for the steady-state value of n_{sj} , we get:

$$n_{sj} = - \frac{c_j}{\xi_j - \frac{1}{\tau_j}}$$

Considering a collection efficiency c' , the Stokes emission intensity can thus be written as:

$$I_{out,j} = \frac{c'n_{sj}}{\tau_j}$$

This model is used to fit the intensity data shown in Fig. 3. We obtain the ratios among the four Raman gain tensor elements. The experimental constants and parameter values obtained from fitting are given in Extended Data Table 1.

Note S3(b). Power dependence and β factor of zero threshold Raman laser

To explain the observed linear power dependence (shown in Fig 2(b)), of the zero-threshold laser for d_1 polarized pump with pump photon number $n_l = n_{l1}$, we take the approximation $n_{l2} \sim 0$ and consider the rate equation of the co-polarized Stokes mode ($n_s = n_{s1}$), which experiences much greater gain ($\xi_1 \gg \xi_2$).

By taking a large photon number approximations in the beginning of the microscopic model it can be shown that above equation (4) can have an alternative and simplified form:

$$\frac{dn_s}{dt} = [\beta F_1 g_{11} n_l - \frac{1}{\tau_1}] n_s$$

Where, a factor β is introduced in the 1st term at the right-hand side to take into account the spectral overlap [7–12] of the Raman and the cavity mode.

Also, the time evolution of the pump photon number n_l can be written as,

$$\frac{dn_l}{dt} = P_{in} - \beta F_1 g_{11} n_l n_s - (1 - \beta) \gamma n_l$$

Here, P_{in} , γ is the generation rate and the scattering rate from pump photon to the cross-polarized Stokes modes, or other radiative and non-radiative processes.

By finding the steady-state solutions of the above system of equations, we find the output intensity is directly proportional to P_{in} , for $\beta=1$:

$$I_{out} = \frac{c' n_s}{\tau} \propto c P_{in}$$

Note S4. Comparison between Conventional laser and Polariton Raman Laser

In a conventional laser, multiple cavity modes exist within a single emission profile in the frequency domain, i.e., different frequencies cavity modes linewidth $\Delta\omega_c$ is much narrower than the emission linewidth (gain profile linewidth) $\Delta\omega$ as shown on the left in Fig. S10. Consequently, there is competition among different cavity modes for pump photons. Therefore, by definition, for multimode lasing, spontaneous emission coupling (β) factor for each cavity modes become less than unity.

$$\beta_i = \frac{\int C_i(\omega - \omega_i) E(\omega) d\omega}{\sum_j \int C_j(\omega - \omega_j) E(\omega) d\omega}$$

However, in our case, polariton modes are playing the role of the cavity modes, while the Raman modes' profile operates as an emission profile. Thus, we find ourselves in the opposite limit of the conventional laser case. Specifically, the emission linewidth (individual Raman modes) ($\Delta\hbar\omega \sim 0.1$ meV) is much narrower than the cavity modes' linewidth ($\Delta\hbar\omega_c \sim 22$ meV) [shown on the right in Fig S10]. Consequently, it becomes a single mode laser for individual Raman frequencies which shows up as zero-threshold laser in the PT-symmetry broken phase i.e. $\xi_1 \gg \xi_2$ with $\beta_i = 1$. The system can also be viewed as a collection of single mode lasers at different frequencies. This is the rationale used to treat the individual Raman modes separately in the above rate equation model.

Table S1: Parameter values obtained from fitting pump dependence at 4K and room temperature

Experimental constants (temperature independent):

$$\lambda (A_g^{12}) = 0.8128 \mu\text{m}, L_{\text{SiO}_2} = 250 \text{ nm}, L_{\text{ReS}_2} = 10 \text{ nm}, n = \frac{n_{\text{SiO}_2} L_{\text{SiO}_2} + n_{\text{ReS}_2} L_{\text{ReS}_2}}{L_{\text{SiO}_2} + L_{\text{ReS}_2}} = 1.88,$$

$$V_{\text{eff}} = \text{Sample area} \times L_{\text{ReS}_2} = 0.01 \mu\text{m}^3.$$

Formulae used:

$$\tau = \frac{Q}{\omega_s} \frac{(\Delta\omega_c)^2}{4(\omega_s - \omega_c)^2 + (\Delta\omega_c)^2}; F = \frac{3Q\left(\frac{\lambda}{n}\right)^3}{4\pi^2 V_{\text{eff}}} \times \frac{(\Delta\omega_c)^2}{4(\omega_s - \omega_c)^2 + (\Delta\omega_c)^2};$$

Cavity parameters obtained from angle resolved reflectivity data (temperature dependent):

Temp	$\Delta\omega_c$ (meV)	ω_{c1} (meV)	ω_{c2} (meV)	ω_s (meV)	Q ₁	Q ₂	τ_1 (ps)	τ_2 (ps)	F ₁	F ₂
10K	10	1.530	1.564	1.526	153.0	156.4	0.23	0.007	53.1	1.6
300K	20	1.548	1.548	1.538	77.4	78.1	0.10	0.031	7.9	3.4

Raman gain tensor ratios obtained from the fitting of experimental data with theory:

Temp	$\frac{g_{22}}{g_{11}}$	$\frac{g_{12}}{g_{11}}$	$\frac{g_{21}}{g_{11}}$
10K	2.52	0.22	0.43
300K	1.67	0.40	0.23

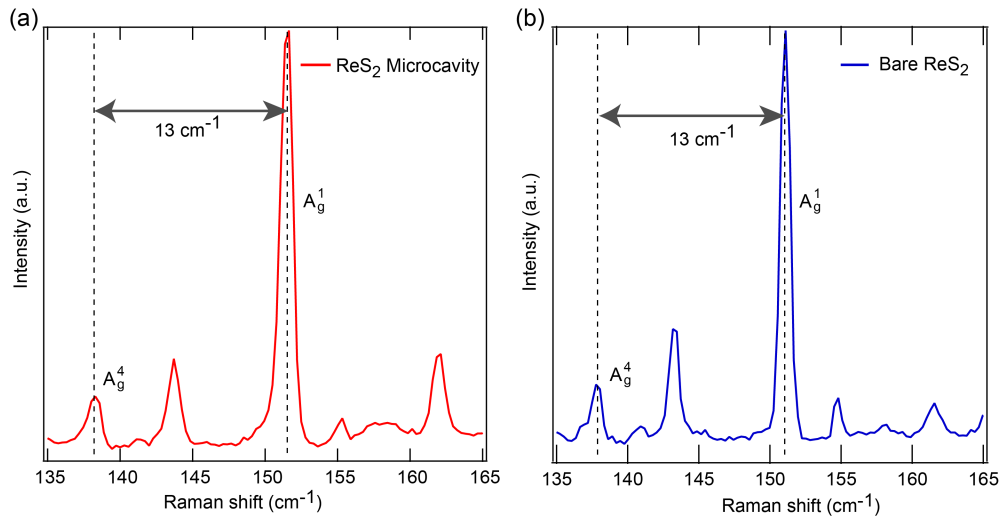


Fig. S1 | Stacking order dependent Raman modes in ReS₂. The A_g^4 and A_g^1 Raman modes exhibit a separation of 13 cm^{-1} indicating AA stacking in both scenarios: (a) ReS₂ within the microcavity and (b) ReS₂ on SiO₂/Si

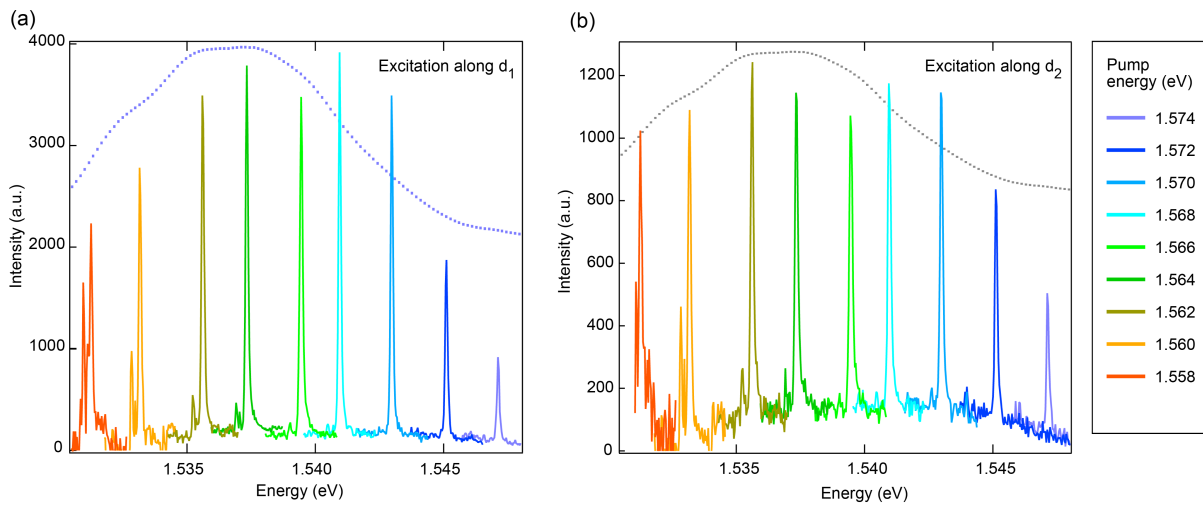


Fig. S2 | Intensity variation of A_g^7 as a function of pump energy. (a) For d_1 excitation, the intensity of the A_g^7 mode (represented with different colors for different excitation energy) becomes maximum when it coincides with the minima of the reflectance dip of L₁. (b) For excitation along d_2 , a similar intensity variation pattern has been observed following the L₁ polariton branch instead of L₂. The absolute reflectance dip from Fig 2(a) has been inverted as a visual aid with blue and black dots in the background in both figures.

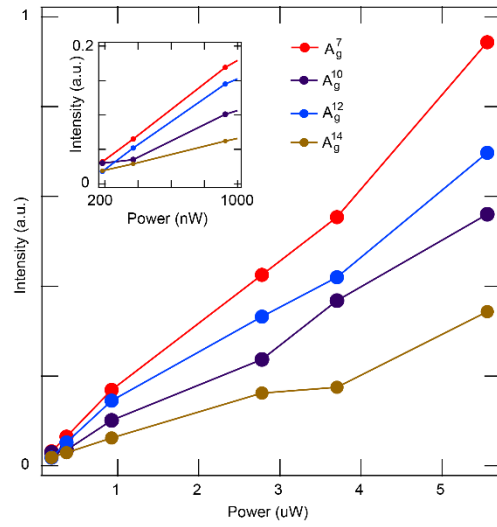


Fig. S3 | Threshold scan in hundreds of nW range for the case of zero threshold lasing when pump beam polarization is along d_1 .

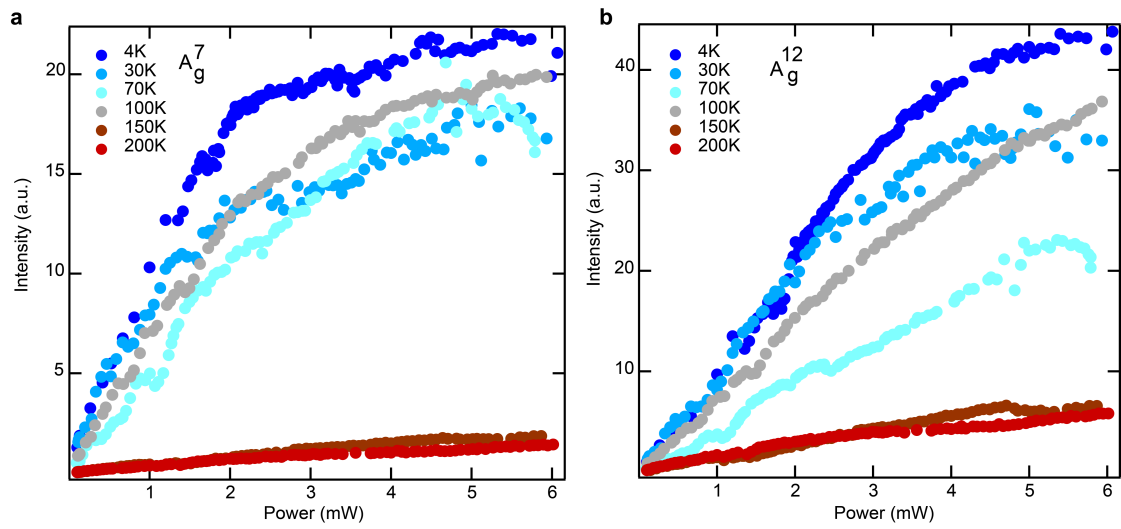


Fig. S4 | Evolution of power dependence with temperature for a. A_g^7 and b. A_g^{12} modes for d_1 polarized pump.

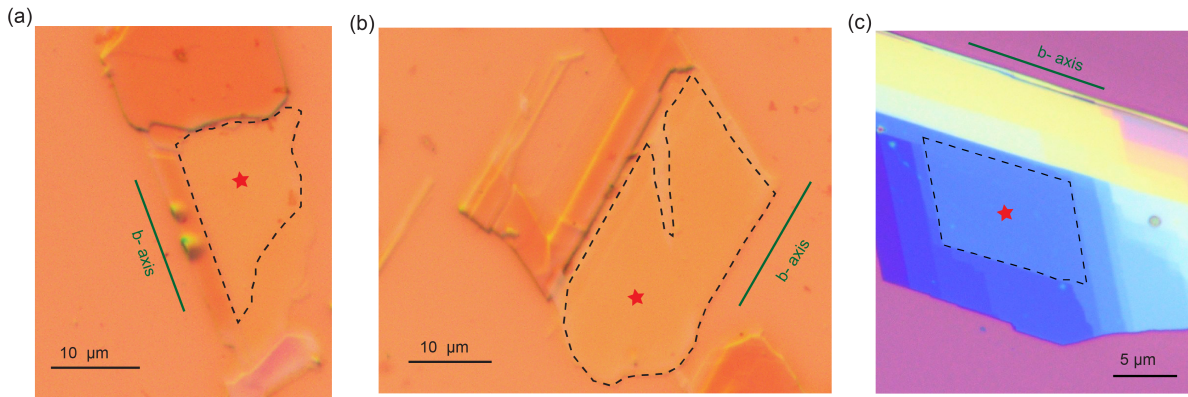


Fig. S5 | Optical microscope images of (a) ReS₂ inside microcavity. All data presented in Figs. 1-4 in the article correspond to experiments done on this sample. (b) Different ReS₂ samples inside microcavity with same thickness as (a) whose corresponding experimental data is shown in fig S8. (c) Bare ReS₂ (ReS₂ on SiO₂/Si). The black dotted lines indicate the boundary of the sample section that is 10 nm in thickness. The red starting point denotes the excitation point.

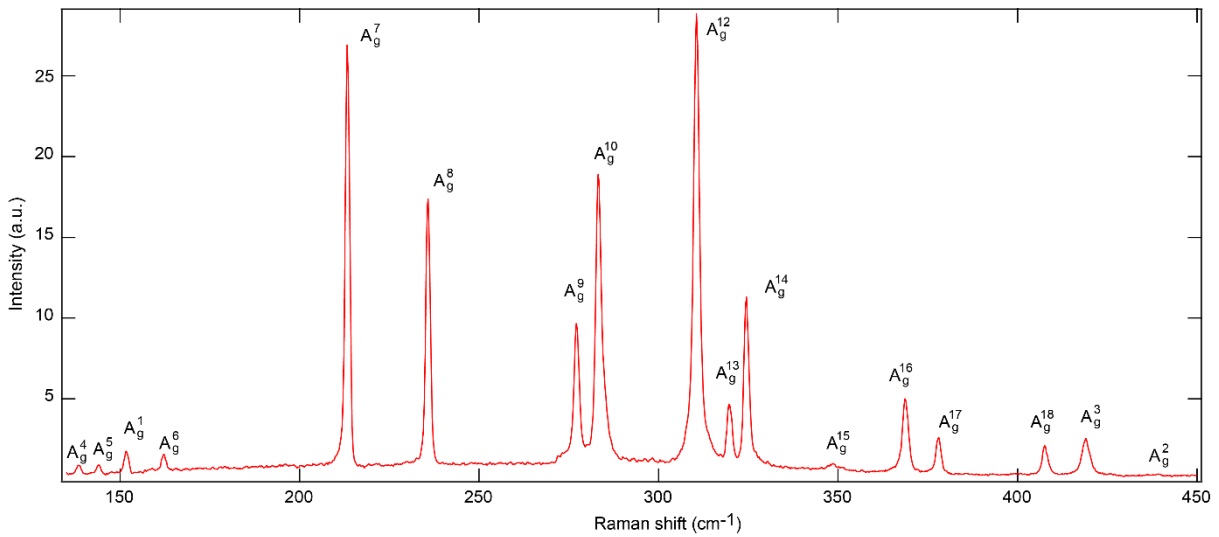


Fig. S6 | Stokes Raman spectra measured for ReS₂ inside microcavity, with the distinct modes labelled.

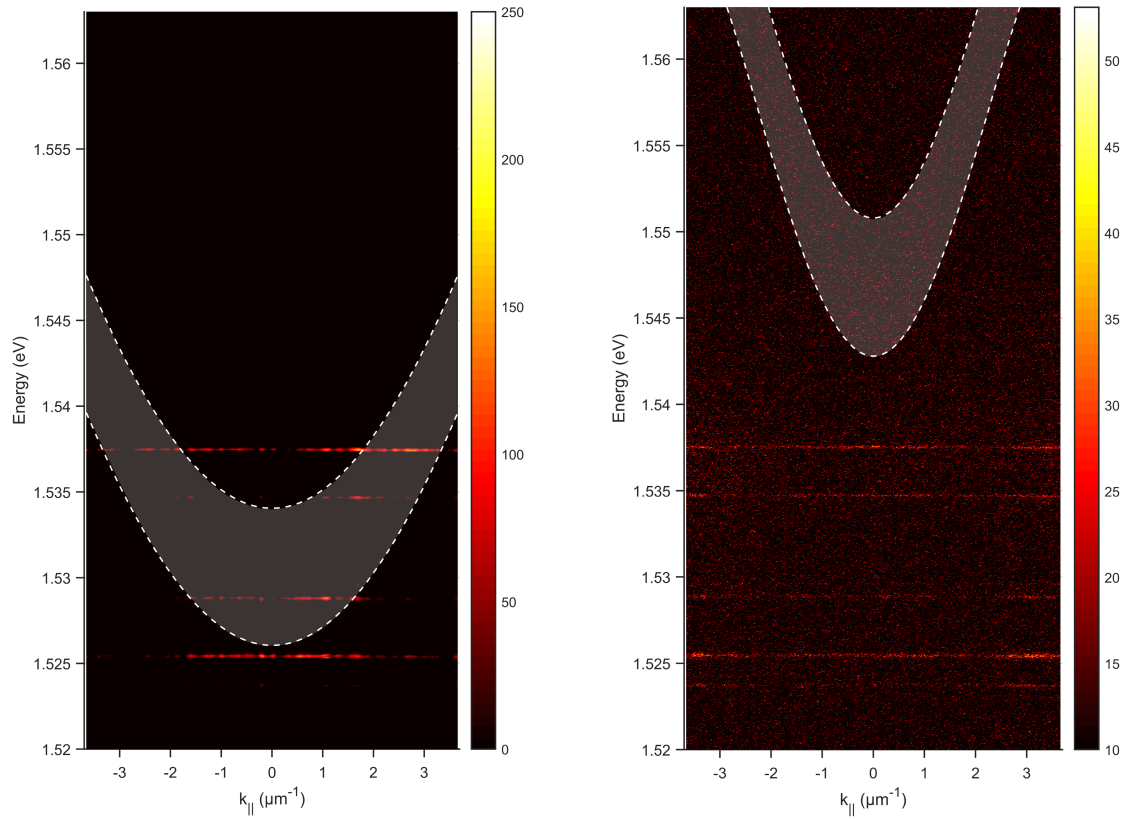


Fig. S7 | Directionality of the lasing emission from the Stokes polariton modes (a) The angle-resolved Raman spectra plots display the Stokes polariton modes profiles, superimposed with the polariton band linewidth from the angle-resolved reflectance spectra (full-width half maxima indicated by the translucent grey region). The figure highlights the A_g^7 , A_g^{10} , A_g^{12} and A_g^{14} modes, which exhibit lasing emission and fulfil the momentum matching condition. (b) Those same Stokes polariton modes do not lase along the d_2 axis do not display any emission pattern.

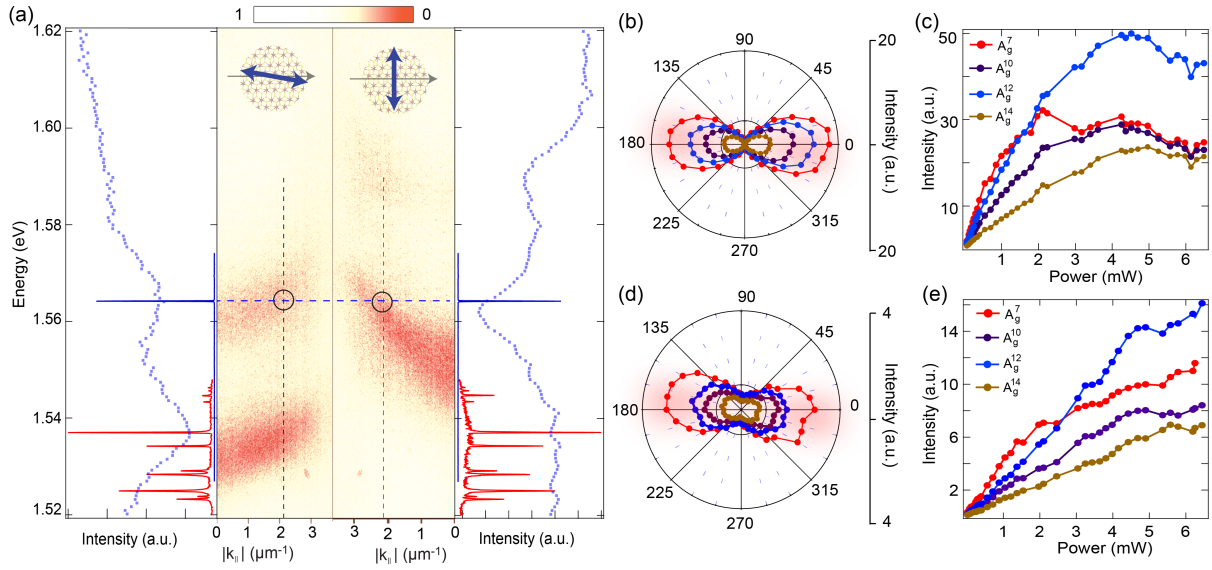


Fig. S8 | Experimental results for alternative sample shown in Extended Data Fig. 5. (a) Angle resolved reflectance for probe beam polarization along d_1 (right) and d_2 (left) axis. EP regions in polariton dispersion for this sample are marked (black circles). Adjacent plots along the extreme left and extreme right show corresponding line profile at the EPs, and the Stokes polariton modes (red) when the pump beam (blue) is polarized along those directions. (b) Polar plot of emission intensity as a function of analyser angle for the pump beam polarization along d_1 , showing a strongly polarized emission. (c) Power dependence data for excitation along d_1 showing ZTPRL for all the Stokes polariton modes. (d) A similar polar plot as figure (b) with the pump polarization beam along d_2 . (e) The power dependence plot showing the finite threshold lasing behavior with a kink near 2 mW for A_g^{10} , A_g^{12} and A_g^{14} with pump polarization along d_2 .

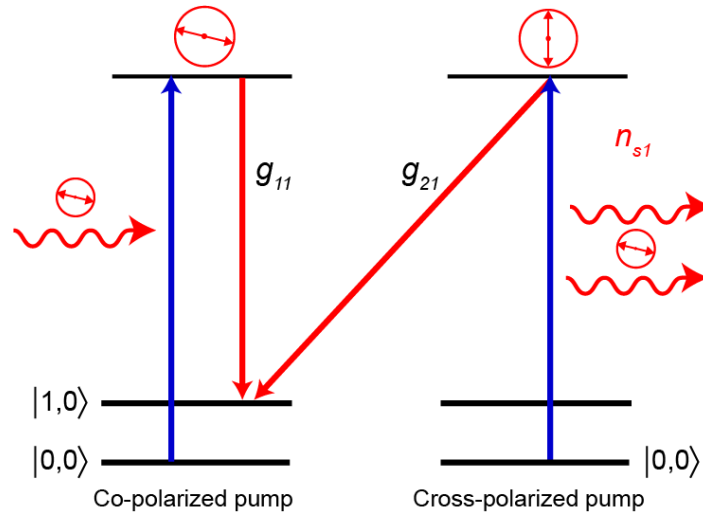


Fig. S9 | Schematic of the stimulated Raman scattering processes. Two possible scattering mechanisms for generation of one of the polarized Stokes modes by co-polarized and cross polarized pump considered in the microscopic model.

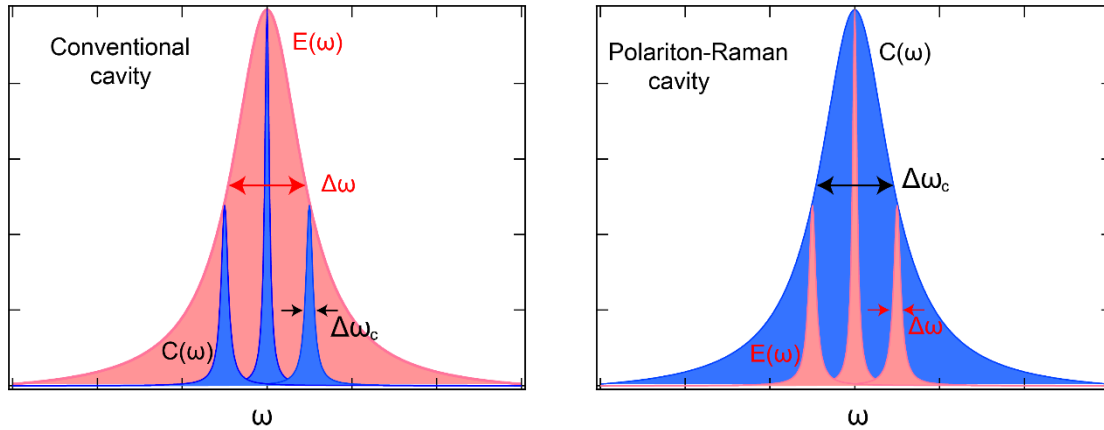


Fig S10 | Gain profile and cavity modes in a conventional laser (left) vs Polariton-Raman laser (right).

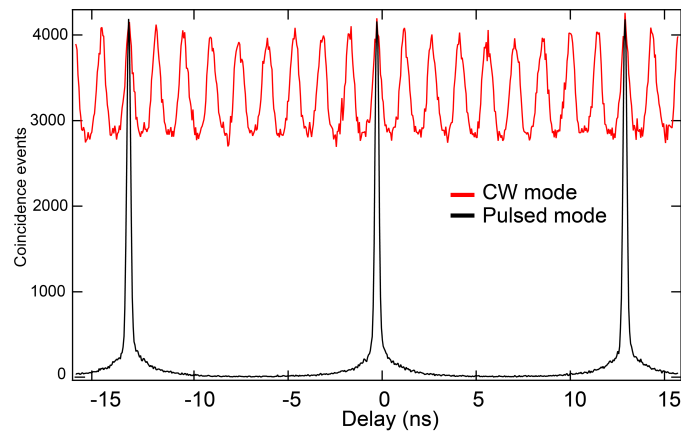


Fig. S11 | Coincidence events recorded using HBT setup to measure second-order correlation, for the pump laser in CW mode (red) and picosecond pulsed mode (black).

References

- [1] A. K. Pattanayak, P. Das, A. Dhara, D. Chakrabarty, S. Paul, K. Gurnani, M. M. Brundavanam, and S. Dhara, *A Steady-State Approach for Studying Valley Relaxation Using an Optical Vortex Beam*, *Nano Lett.* **22**, 4712 (2022).
- [2] D. Chakrabarty, A. Dhara, P. Das, K. Ghosh, A. R. Chaudhuri, and S. Dhara, *Anisotropic Exciton Polariton Pairs as a Platform for PT-Symmetric Non-Hermitian Physics*, arXiv:2305.17472.
- [3] A. McCreary, J. R. Simpson, Y. Wang, D. Rhodes, K. Fujisawa, L. Balicas, M. Dubey, V. H. Crespi, M. Terrones, and A. R. Hight Walker, *Intricate Resonant Raman Response in Anisotropic ReS₂*, *Nano Lett.* **17**, 5897 (2017).
- [4] Y. Zhou et al., *Stacking-Order-Driven Optical Properties and Carrier Dynamics in ReS₂*, *Adv. Mater.* **32**, 1908311 (2020).
- [5] A. Yariv, *Quantum Electronics*, 3rd ed (Wiley, New York, 1989).

- [6] Y. Wu, X. Yang, and P. T. Leung, *Theory of Microcavity-Enhanced Raman Gain*, Opt. Lett., OL **24**, 345 (1999).
- [7] H. Yokoyama and S. D. Brorson, *Rate Equation Analysis of Microcavity Lasers*, Journal of Applied Physics **66**, 4801 (1989).
- [8] X. Checoury, Z. Han, M. El Kurdi, and P. Boucaud, *Deterministic Measurement of the Purcell Factor in Microcavities through Raman Emission*, Phys. Rev. A **81**, 033832 (2010).
- [9] G. Bjork and Y. Yamamoto, *Analysis of Semiconductor Microcavity Lasers Using Rate Equations*, IEEE J. Quantum Electron. **27**, 2386 (1991).
- [10] B. Petrak, N. Djeu, and A. Muller, *Purcell-Enhanced Raman Scattering from Atmospheric Gases in a High-Finesse Microcavity*, Phys. Rev. A **89**, 023811 (2014).
- [11] A. V. Kavokin, J. Baumberg, G. Malpuech, and F. P. Laussy, *Microcavities*, Second edition (Oxford University Press, Oxford, 2017).
- [12] J. B. Khurgin and M. A. Noginov, *How Do the Purcell Factor, the Q -Factor, and the Beta Factor Affect the Laser Threshold?*, Laser & Photonics Reviews **15**, 2000250 (2021).